Review of Materials Research 1 (2025) 100005

Contents lists available at ScienceDirect

Review of Materials Research

journal homepage: www.sciencedirect.com/journal/review-of-materials-research

Space station based experimental research on thermophysical properties and solidification mechanisms of Fe-19%Si alloy

L. Hu, W.J. Xie, Z.X. Wan, Q.C. Zhong, Y.H. Jing, H.P. Wang *

School of Physical Science and Technology, Northwestern Polytechnical University, Xi'an, 710072, China

A B S T R A C T

The thermophysical properties and rapid solidification mechanism of Fe-19 wt%Si alloy were investigated by electrostatic levitation aboard China Space Station and terrestrial drop tube techniques. All the solidification events neither favour the retention of the metastable Fe_2Si phase nor induce the decomposition of the Fe_5Si_3 phase. The density was determined to be a linear decreasing relationship with temperature, in which the liquid density at eutectic temperature was determined to be 6.19 g cm^{-3}. The surface tension and viscosity were measured to be 1.44 N m^{-1} and 29.8 mPa s at liquid state. Because space environment suppresses the gravity-driven liquid flow required for solidification feeding, the space shrinkage was significantly higher than the ground condition. The Fe_3Si and Fe_2Si phases only displayed a divorced eutectic growth mode in the ground-based experiments, while the coupled growth appears under the space condition due to the suppression of long-range solute transport. The crystal grain size of Fe_3Si phase in space condition was larger than that on the ground.

1. Introduction

For metallic materials, the final performances are largely dependent on their solidification microstructures. The morphological evolution of microstructures during solidification has attracted significant attention from both academic research and industrial applications [1]. The current studies indicate that the convection induced by gravity has a strong effect on the microstructure and chemical segregation [2,3]. When the gravity-driven phenomena such as sedimentation, natural convection, and hydrostatic pressure are suppressed, the conditions become favourable for investigating purely diffusion-controlled solidification [4,5]. Eutectic alloys, in which solidification heavily relies on solute diffusion, have been the focus of numerous studies in microgravity experiments, especially in the context of directional solidification [5–8]. Under directional solidification in space, eutectic spacing is reduced due to the suppression of mass transport in the melt [2]. The eutectic growth direction tends to tilt towards the downstream side of the fluid flow [6]. Both rod-like and lamellar eutectics have been observed during directional solidification in space [7]. Moreover, the original coupled growth of eutectic phases has unexpectedly been found to exhibit a decoupled growth mode when undercooling reaches 18% of the eutectic temperature T_E [8]. Therefore, the influence of microgravity on solidification requires further investigation, particularly in the context of space exploration.

The Fe-Si alloys, which possess excellent soft magnetic properties, have been widely applied in energy-saving transformers and electric motor vehicles [9]. As a compound-forming system, they exhibit several distinct solid solution and intermetallic phases [10]. In the Fe-19%Si eutectic alloy, the ordered solid solution Fe_3Si and the intermetallic Fe_2Si phase are derived from the eutectic reaction, with both phases demonstrating good ferromagnetic performance. However, whether the soft ferromagnetic Fe_2Si intermetallic phase can be retained through rapid solidification requires further experimental investigation [11]. The influence of microgravity on the microstructure of Fe_3Si and Fe_2Si phases has not yet been explored. Additionally, accurate thermodynamic properties are important for the silicon steel and ferrosilicon alloy production chain [12].

In this work, we investigated the solidification mechanism of the Fe-19%Si eutectic alloy using electrostatic levitation (ESL) experiments conducted aboard the China Space Station (CSS) and on the ground. The thermophysical properties were measured aboard the CSS to provide fundamental data [13–16].

2. Experimental procedure

The Fe-19%Si alloy samples, with diameters of approximately 2.7 mm (~70 mg in mass), were prepared from high-purity component metal slugs: Fe (99.95% purity) and Si (99.9999% purity), both sourced from Alfa Aesar, using the arc-melting method. The alloy samples were then sent to the CSS aboard the Tianzhou spacecraft. More details about the ESL experiments conducted aboard the CSS are available elsewhere [8,17]. To ensure the comparability of experimental results, terrestrial ESL

* Corresponding author.
E-mail address: hpwang@nwpu.edu.cn (H.P. Wang).

https://doi.org/10.1016/j.revmat.2025.100005
Received 21 March 2025; Received in revised form 1 April 2025; Accepted 1 April 2025
Available online 7 April 2025

experiments [13,18,19] were conducted using the same batch of samples as those used in the CSS experiments. The samples were melted using focused laser beams and then allowed to cool naturally by turning off the laser power. The sample temperature was monitored using a two-colour pyrometer. A CCD camera, coupled with a UV backlight, was employed to capture the projection of the sample. The density ρ was determined using the formula $\rho = m/V$, where m is the sample mass. Mass loss can be ignored during the ESL experiments. Details on the determination of V can be found in Ref. [20]. The density was also measured under terrestrial conditions. The surface tension σ_L and viscosity η_L of the liquid alloy were determined using the droplet oscillation method under ground ESL conditions [14].

The drop tube technique was also adopted to explore the rapid solidification mechanisms under much higher undercooling and cooling rate than ESL. The cooling rate and diameter of alloy droplets are about 10^3~10^4 K/s and 10–1000 μm, respectively. To investigate the solidification shrinkage behaviour, a Zeiss Xradia 620 Versa high-resolution 3D X-ray tomography microscope was used to detect the porosity of samples solidified under different conditions [21]. Phase transitions were studied using a Netzsch DSC 404 differential scanning calorimeter (DSC) at a constant heating rate of 20 K/min. Following the ESL and drop tube experiments, the samples were sectioned and polished according to standard metallographic procedures. The microstructure was analysed using an FEI Sirion200 scanning electron microscope (SEM) equipped with an Oxford energy disperse spectroscopy (EDS) and Nordlys electron backscattered diffraction (EBSD) system. The phase constitution was confirmed using a Bruker D8 X-ray diffractometer (XRD).

3. Results and discussion

3.1. Electrostatic levitation processing aboard CSS

According to the latest Fe-Si binary alloy phase diagram [11] shown in Fig. 1a, two kinds of ordered solid solution phases with different crystal structures exist: α′-FeSi (B2 type) and α″-Fe_3Si ($D0_3$ type). In addition, the Fe-19%Si eutectic alloy undergoes three phase transition processes. First, the liquid phase undergoes an invariant eutectic reaction L→Fe_3Si + Fe_2Si at 1475 K. This is followed by a eutectoid decomposition Fe_2Si→Fe_3Si + Fe_5Si_3 at 1321 K. Subsequently, a second eutectoid reaction occurs, Fe_5Si_3→Fe_3Si + FeSi at 1099 K. The final microstructure should consist of Fe_3Si and FeSi phases. However, the DSC analysis (Fig. 1b) detects only the eutectic reaction at T_E = 1472 K and the first eutectoid decomposition at 1281 K. The microstructure shown in Fig. 1c and the XRD pattern (Fig. 1d) of the master alloy indicate that, under near-equilibrium conditions, the microstructure is composed of Fe_3Si and Fe_5Si_3 phases. The Fe_2Si eutectic phase is completely consumed, and the eutectoid decomposition of the Fe_5Si_3 phase does not occur. Furthermore, under ESL conditions aboard the space station and on the ground, and under drop tube condition, the phase constitutions at various undercoolings and cooling rates are consistent with those of the master alloy. This suggests that, for the Fe-19%Si alloy, rapid solidification from the undercooled liquid state neither favours the retention of the soft ferromagnetic Fe_2Si phase nor induces the decomposition of the Fe_5Si_3 phase. The preservation of Fe_2Si phase may need a much higher cooling rate or undercooling.

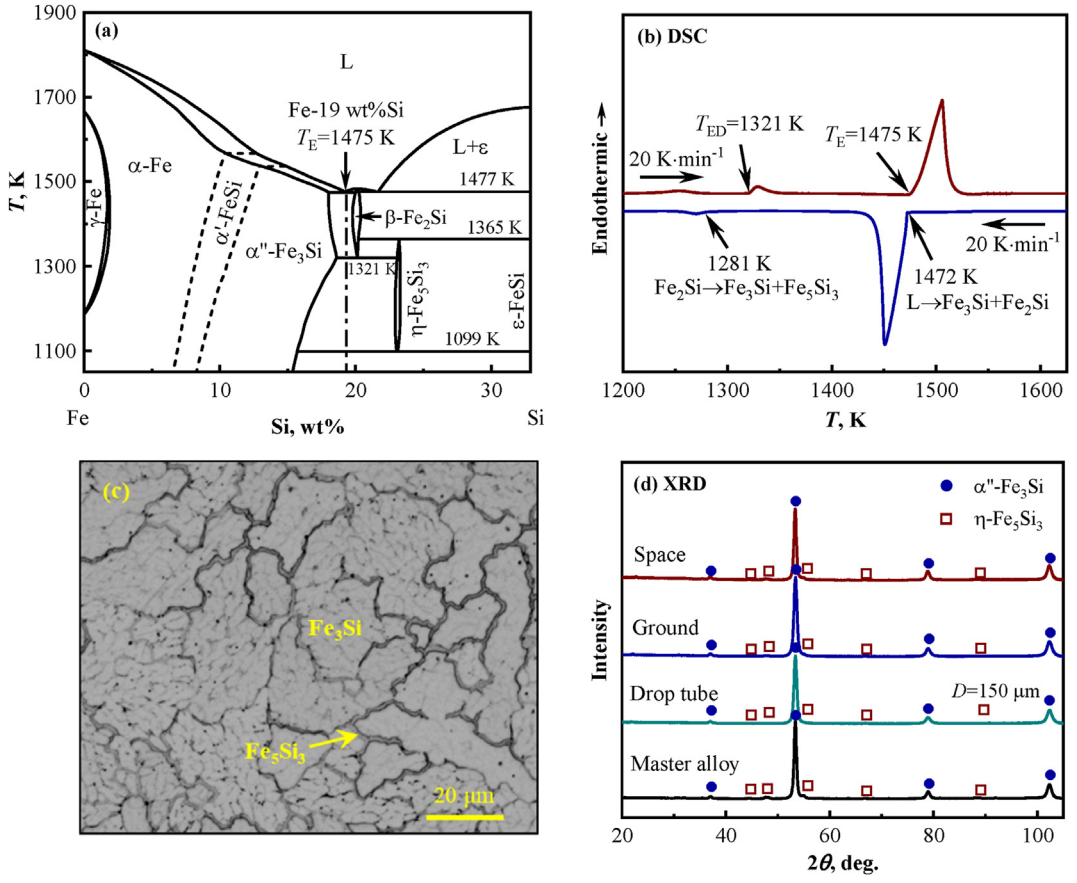

Fig. 1. Phase constitution analysis of Fe-19%Si alloy: (a) Selection of alloy composition; (b) DSC curve; (c) Microstructure of master alloy; (d) XRD patterns of space and ground samples.

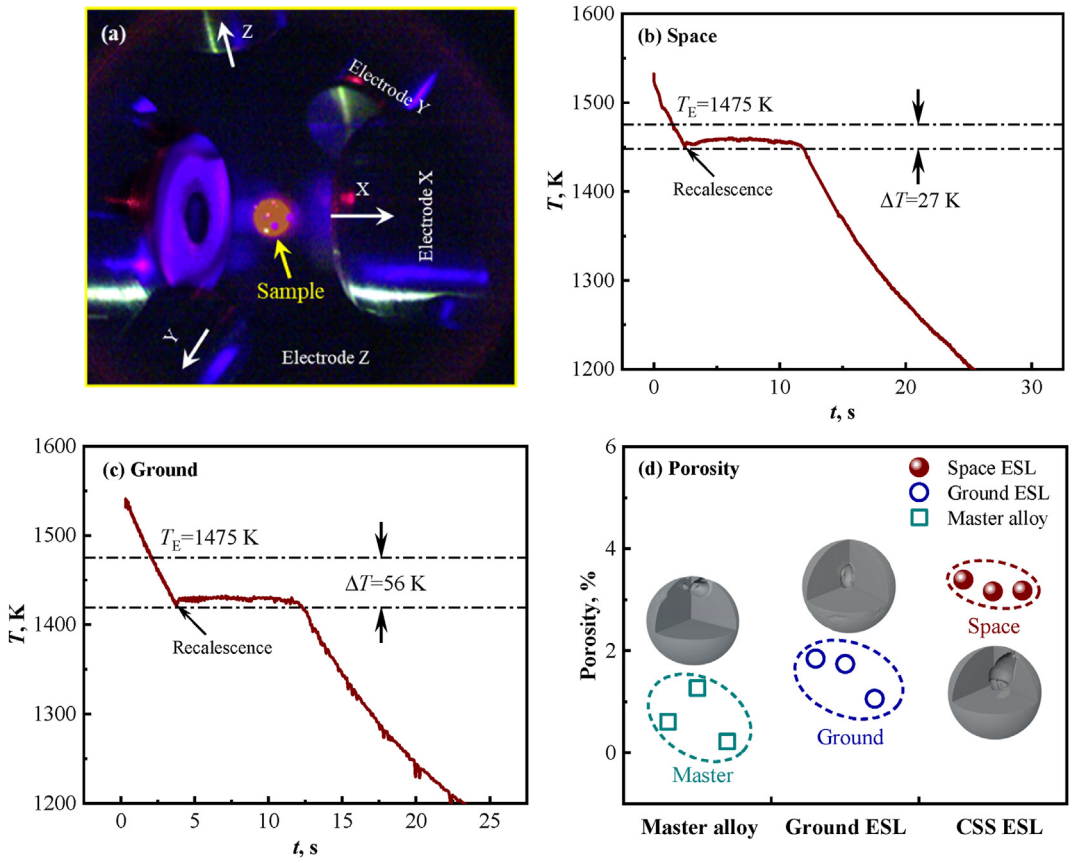

Fig. 2. Space solidification process of Fe-19%Si alloy: (a) Electrostatic levitation setup aboard space station; (b) Cooling curve aboard space station; (c) Cooling curve on the ground; (d) Shrinkage porosity under different conditions.

Fig. 2 presents three pairs of electrodes and a typical temperature curve illustrating the undercooling and solidification processes. By varying the degree of superheating, the liquid alloy was undercooled to different levels. Due to the limited surface charge and its propensity to dissipate during the melting of the Fe-Si alloy, achieving a superheated liquid state in space is challenging. Consequently, the maximum undercooling obtained in space $\Delta T = 27$ K is only half of that achieved on the ground ($\Delta T = 56$ K). Both temperature curves in Fig. 2b and c reveal the eutectic reaction L→Fe_3Si + Fe_2Si. However, the subsequent eutectoid decomposition is not reflected in the cooling curves due to the minimal heat release during this process. Furthermore, the average cooling rates in the liquid and solid-states (Fig. 2b) are calculated as 20 K/s and 18 K/s, respectively. These rates are slightly lower than the corresponding cooling rates of 36 K/s and 31 K/s observed on the ground (Fig. 2c).

3.2. Thermophysical properties of liquid alloy

As shown in Fig. 3a and b, the densities in both the liquid and solid-states, measured aboard the space station (ρ_{L1} and ρ_{S1}) and on the ground (ρ_{L2} and ρ_{S2}), decrease linearly with increasing temperature:

$$\rho = \rho_0 + \frac{d\rho}{dT}(T - T_E), \tag{1}$$

where ρ_0 is the density at T_E, and $d\rho/dT$ is the temperature coefficient. For the liquid alloy, the ρ_0 values measured in space and on the ground are 6.19 and 6.17 g cm^{-3}, respectively. These values are very similar; however, the $d\rho/dT$ value in space (1.48×10^{-3} g cm^{-3} K^{-1}) is larger than that on the ground (7.36×10^{-4} g cm^{-3} K^{-1}). Fig. 3a also indicates that the superheated temperature range on the ground is much larger than that in space, leading to a higher undercooling. As shown in Fig. 3b, the ρ_0 values for the solid-state are 6.40 g cm^{-3} in space and 6.24 g cm^{-3} on the ground. The relative solidification shrinkage δ can be calculated by [22].

$$\delta = (V_L - V_S) / V_L, \tag{2}$$

where V_L and V_S are the sample volumes at T_E temperature for the liquid and solid-states, respectively. The δ for the sample solidified in space is 3.28%, while that for the sample on the ground is 1.12%.

Furthermore, the surface tension σ_L (Fig. 3c) also shows a linear decrease with increasing temperature, described by

$$\sigma_L = \sigma_0 + \frac{d\sigma}{dT}(T - T_E). \tag{3}$$

The σ_0 of the liquid alloy at T_E and its temperature coefficient $d\sigma/dT$ are derived to be 1.44 N m^{-1} and -4.35 × 10^{-4} N m^{-1} K^{-1}, respectively. As shown in Fig. 3d, the dependence of liquid viscosity η_L on temperature follows the Arrhenius equation [14,23].

$$\eta_L = \eta_0 \exp(Q / R_g T), \tag{4}$$

where η_0 is a constant, R_g is the gas constant, and Q is the activation energy, which was determined to be 34.9 kJ/mol. Consequently, the liquid viscosity at T_E was measured to be 29.8 mPa s.

3.3. Microstructure and solute distribution

The X-ray tomography analysis in Fig. 2d reveals the internal porosity of the final sample after solidification, followed by a eutectoid decomposition. As shown in the insert images, notable cavities are distributed within the samples. The porosity percentage of the arc-melted master sample is approximately 1%. In comparison, ESL-solidified samples exhibit a higher porosity percentage (1–4%). Under containerless

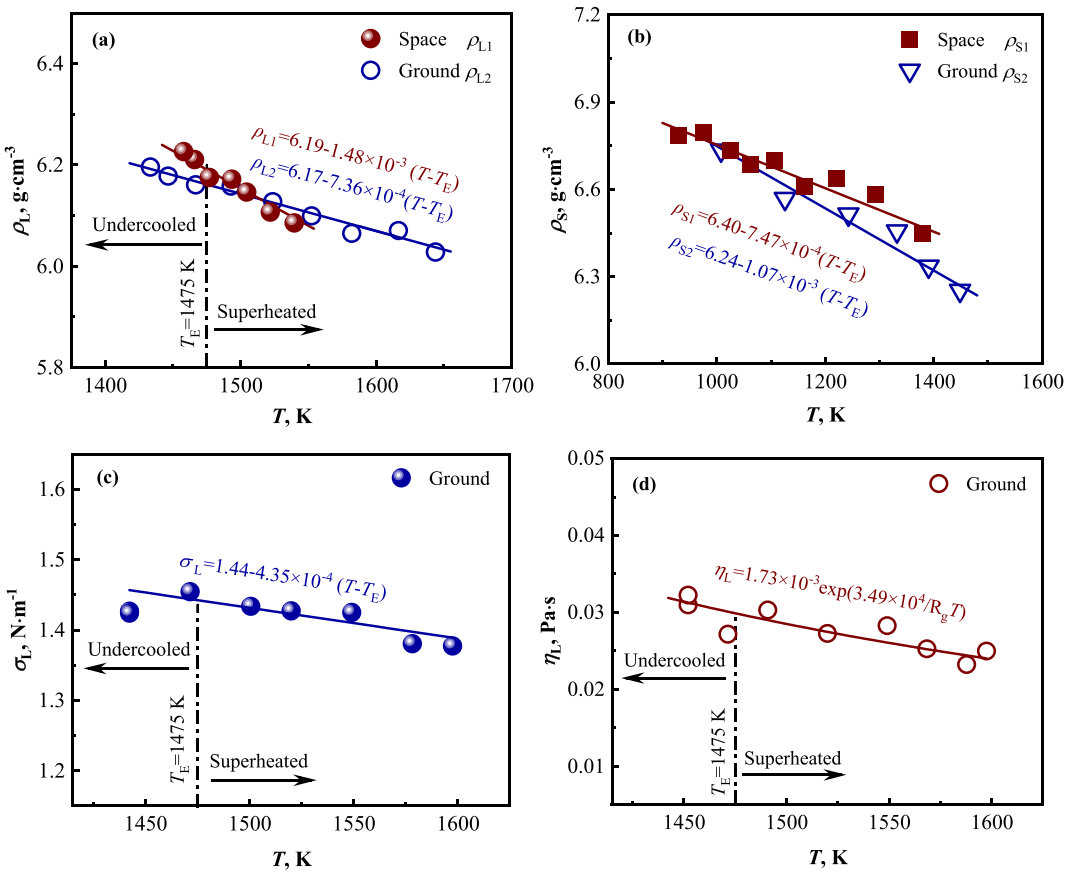

Fig. 3. Thermophysical properties of Fe-19%Si alloy measured in space versus ground results: (a) Liquid density; (b) Solid density; (c) Liquid surface tension; (d) Liquid viscosity.

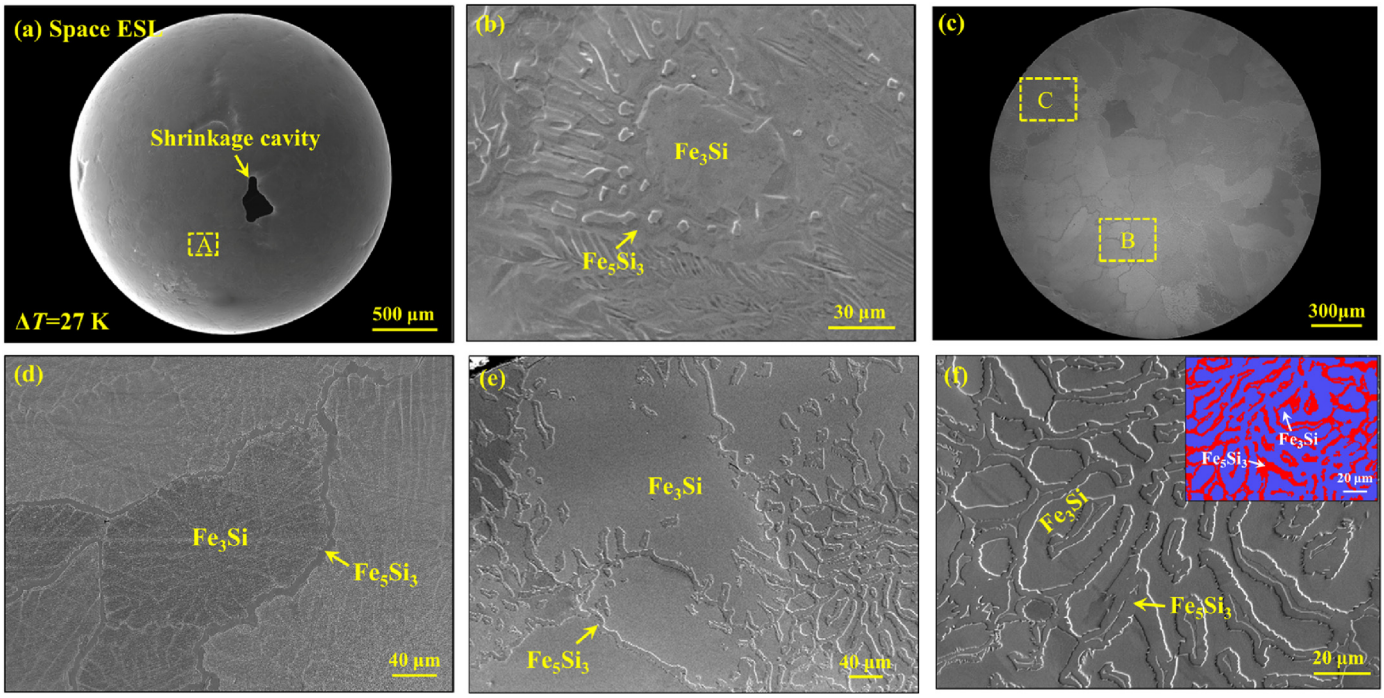

Fig. 4. Structural morphology of Fe-19%Si alloy solidified aboard space station: (a) Surface microstructure; (b) Enlarged view of frame A; (c) Internal microstructure; (d, e) Internal microstructure of frame B and C; (f) Partial enlarged view of frame C inserted with EBSD pattern of phase distribution.

conditions, solidification typically begins at the sample surface, which experiences the highest temperature gradient, resulting in shrinkage cavities retained within the sample. Furthermore, the porosity percentage of the sample solidified in space is 3–4% significantly higher than that of the sample solidified on the ground (1–2%). These results align well with the solidification shrinkage data derived from the density measurements in Fig. 3. It is suggested that the internal porosities are mainly caused by solidification shrinkage, while solid-state transformations contribute only a small proportion of the porosity [21]. Additionally, the space environment suppresses the gravity-driven liquid flow required for solidification feeding, leading to a higher percentage of porosity [24].

Figs. 4 and 5 present the microstructure and EBSD analyses of the phase distribution in the sample solidified at $\Delta T = 27$ K in the space station and $\Delta T = 30$ K on the ground, respectively. As observed in the surface microstructure in Fig. 4a and the enlarged morphology in Fig. 4b–a distinct dual-phase microstructure of Fe_3Si and Fe_5Si_3 is formed. However, the interior microstructure in Fig. 4c exhibits two typical morphologies. In the interior region, there are coarse crystal grains of Fe_3Si with a small amount of interdendritic Fe_5Si_3 (Fig. 4d). The region near the free surface (Fig. 4e and f) shows a distinct coupled-growth manner. According to the inserted EBSD phase map, where the blue and red phases represent Fe_3Si and Fe_5Si_3, respectively, the fraction of the Fe_5Si_3 phase reaches 33%. More importantly, there are a small amount of Fe_3Si inside the Fe_5Si_3 grains, which results from the decomposition of Fe_2Si phase. Thus, it is the evidence for the coupled growth of Fe_3Si and Fe_2Si phases.

However, the situation on the ground is markedly different. As shown in Fig. 5a and the enlarged image in Fig. 5b, the microstructure on the free surface of the ground-based sample is characterised by numerous equiaxed dendrites of Fe_3Si. The interior microstructure in Fig. 5c further indicates that Fe_5Si_3 distributes in the interdendritic regions, similarly to the master alloy (Fig. 1c) and the interior region of space sample (Fig. 4d). This suggests that Fe_3Si solidified as the primary phase, after which the residual liquid solidified into a small amount of Fe_2Si phase through a process of divorced eutectic growth. Based on the EBSD results, Fe_5Si_3 phase with a relative fraction of only 13% is detected.

Fig. 6 presents the solute distribution of two different regions in the sample solidified at $\Delta T = 27$ K in the space. It can be seen from the line scanning result of line A (Fig. 6c) that the content fluctuation appears at the region near the surface (Fig. 6a). In the interior region in Fig. 6b, according to the line scanning of B (Fig. 6d) and mapping of Si in Fig. 6e, the fluctuation happens in the grain boundary, while no signification fluctuation of Si can be detected inside the Fe_3Si grain. Moreover, the Si content inside Fe_3Si grain was measured to be about 31%, which agrees well with the composition in Fe_3Si phase after a eutectoid reaction at $T =$ 1321 K in phase diagram (Fig. 1a). The derived 38% atomic percent of Si in grain boundary confirms the existence of Fe_5Si_3 phase.

Furthermore, as shown in Fig. 5d–f, the alloy droplets solidified in drop tube exhibit similar morphology to the master alloy and ground ESL sample. According to the calculated undercooling and cooling rate in Fig. 7a, the ΔT and R_c of the smallest alloy droplets (D~150 μm) are obtained to be 113 K and 3.1 × 10^4 K/s, respectively. Even under such high undercooling and cooling rate, the metastable phase Fe_2Si still cannot be retained in the final microstructure. Moreover, the coupled growth morphology of Fe_3Si and Fe_5Si_3 cannot also be found. Therefore, the Fe-19%Si eutectic alloy still solidifies into Fe_3Si and Fe_2Si as a divorced growth manner under such high undercooling and cooling rate conditions.

3.4. Eutectic growth mechanism in space

According to the classic nucleation theory and the models for dendrite and eutectic growth [25,26], the nucleation rates I and growth velocity v

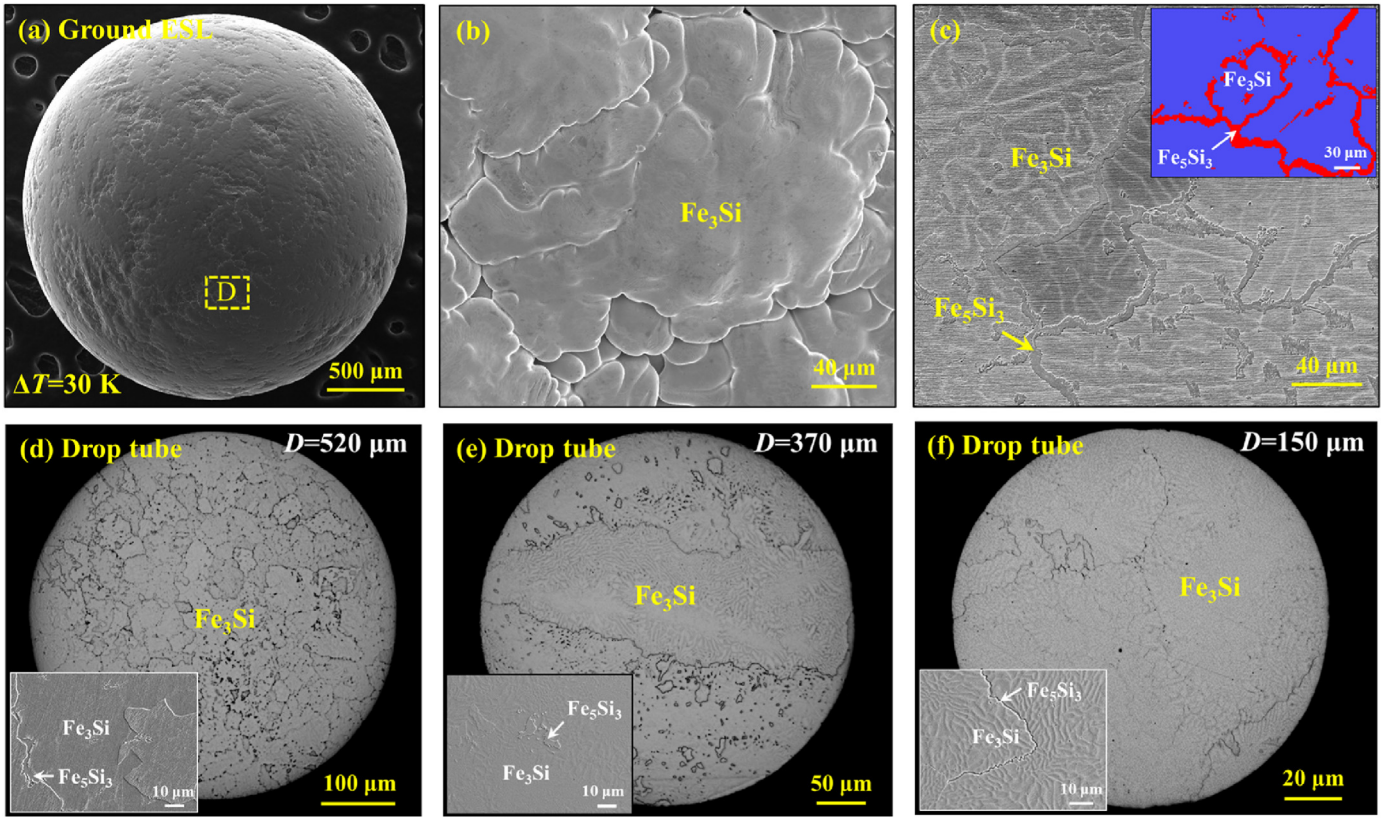

Fig. 5. Structural morphology of Fe-19%Si alloy solidified under ground ESL and drop tube conditions: (a) Surface microstructure; (b) Enlarged view of frame D; (c) Internal microstructure inserted with EBSD pattern of phase distribution; (d, e, f) Internal microstructures of alloy droplets with three different diameters.

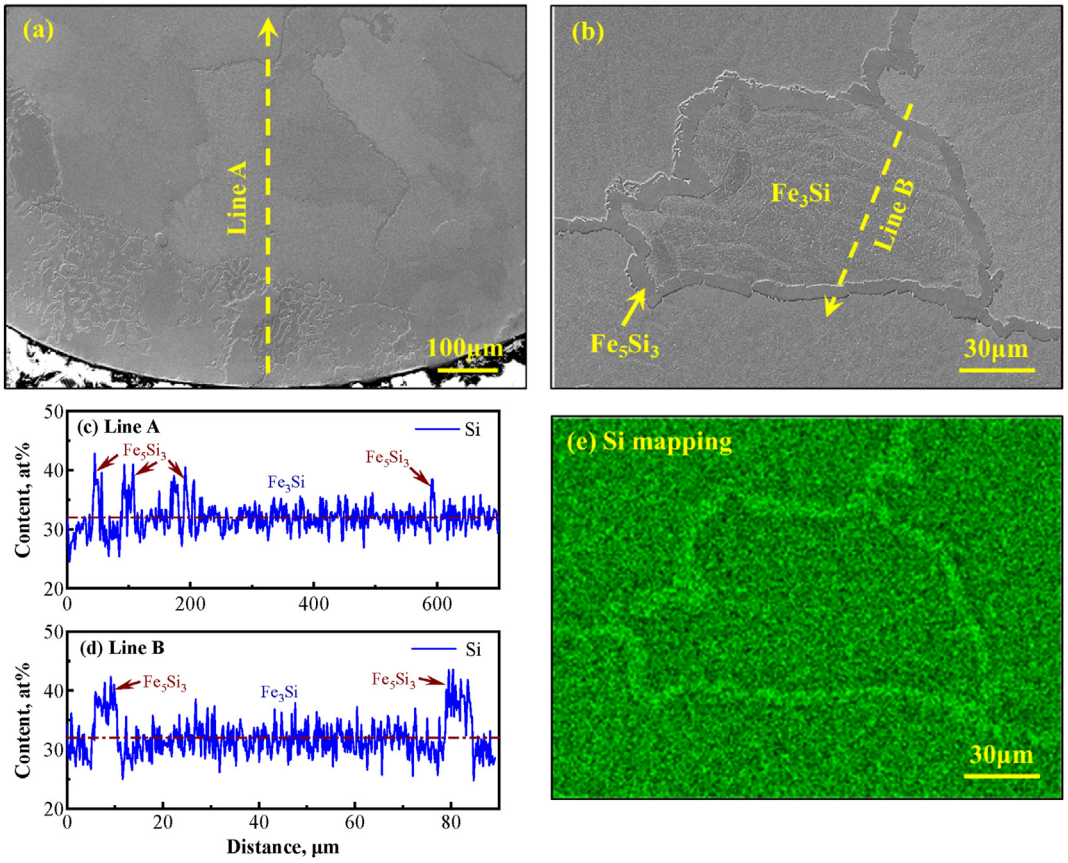

Fig. 6. Component distribution of Fe-19%Si alloy solidified aboard space station: (a, b) Internal microstructure of the sample at $\Delta T = 27$K; (c, d) EDS analysis along line A and B; (e) EDS mapping of solute element Si of enlarged view in (b).

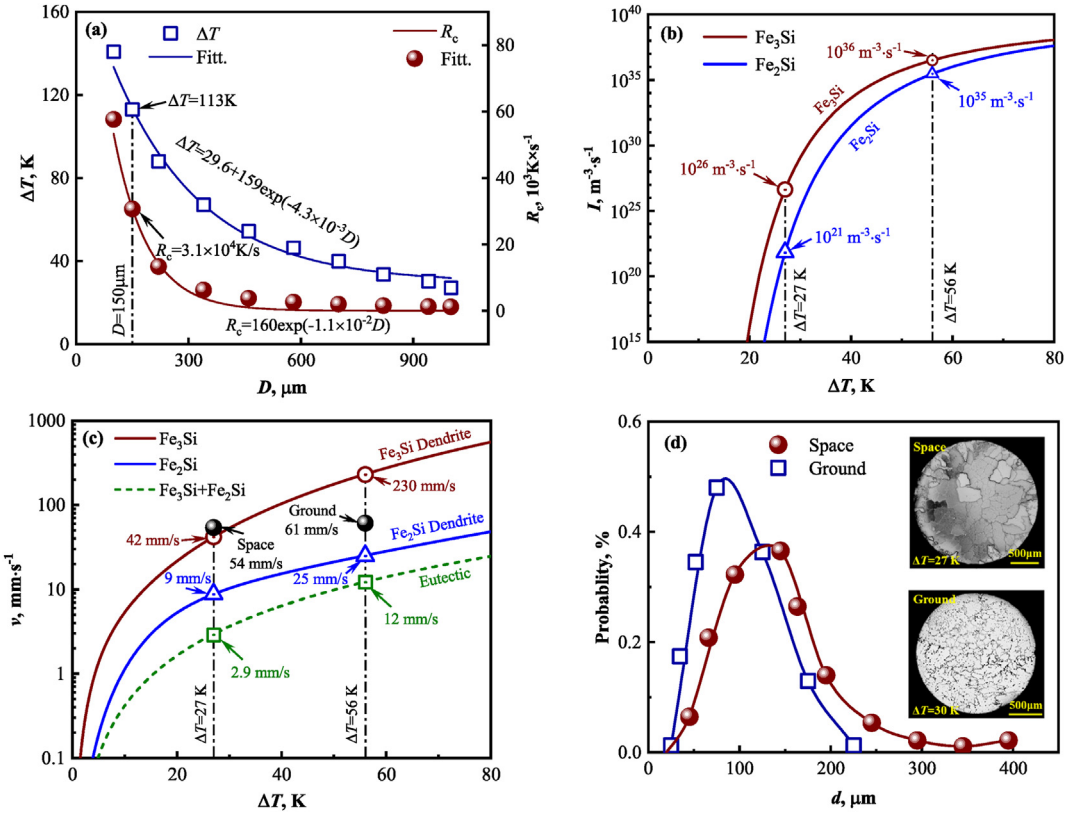

Fig. 7. Crystal nucleation and growth mechanisms: (a) Calculated undercooling and cooling rate under drop tube condition; (b) Calculated nucleation rate of Fe_3Si and Fe_2Si; (c) Calculated dendrite and eutectic growth velocity; (d) Grain size distribution of Fe_3Si under space and ground ESL conditions.

were calculated to reveal the divorced eutectic growth mechanism. It can be inferred from Fig. 7b that the Fe_3Si phase, whose nucleation rate is 1-5 orders of magnitude higher than that of Fe_2Si, acts as the priority nucleation phase in the range of undercooling obtained by experiments. Moreover, the Fe_3Si dendrite apparently grows more rapidly than the Fe_2Si dendrite and Fe_3Si + Fe_2Si eutectic phase (Fig. 7c). As shown in Fig. 7c, according to the measured recalescence time in Fig. 2b and c, the dendrite growth velocity of primary Fe_3Si under the space and ground conditions can be estimated to be 54 mm/s ($\Delta T = 27$K) and 61 mm/s ($\Delta T = 56$K). Therefore, from the perspective of growth kinetics, the Fe_3Si dominates the crystal growth process. These theoretical analyses explain the cause of phase constitution in as-cast alloy, and the samples solidified by ground-based ESL and drop tube well.

Nevertheless, the characteristic divorced eutectic growth is no longer the only mechanism in the space condition, while the coupled growth appears especially on the sample surface. The totally different surface microstructure from ground sample in Fig. 4a and the dual-phase structure in Fig. 4f can prove this point. Under the space ESL condition, natural convection is significantly suppressed [27], and the uniform heating configuration of four lasers further reduces thermal convection. The growth of the primary Fe_3Si phase is restrained due to the significant influence on long-range solute transport. Eutectic growth, which requires only short-range solute diffusion, becomes more pronounced, leading to the formation of a coupled growth microstructure in the surface region. As solidification progresses into the internal region, convection within the sample becomes stronger than at the surface. This results in a microstructure similar to that observed in the terrestrial experiment. These two distinct morphologies therefore underscore the significant effect of convection on eutectic growth.

Another obvious difference between space and ground ESL experiments is the grain size d of Fe_3Si equiaxed dendrites. As seen from grain size distribution in Fig. 7d, the most probable size and the average size of the sample solidified at $\Delta T = 27$ K in the space are larger than the sample solidified at $\Delta T = 30$ K on the ground. It should be attributed to the suppress of natural convection, which is favourable for the diffusion-controlled grain growth.

4. Conclusions

The thermophysical properties and solidification mechanism of Fe-19 wt%Si eutectic alloy were investigated by ESL in space, ground-based ESL and drop tube techniques. The main conclusions are as follows.

(1) All the solidification processes under space and terrestrial conditions neither favour the retention of the metastable Fe_2Si phase nor induce the decomposition of the Fe_5Si_3 phase.
(2) The density was determined to be a linear decreasing relationship with temperature through space station experiments, in which the liquid density at eutectic temperature was derived to be 6.19 g cm^{-3}. The liquid surface tension and liquid viscosity at T_E were measured to be 1.44 N m^{-1} and 29.8 mPa s.
(3) The shrinkage porosity percentage of the sample solidified in the space station is significantly larger than that observed on the ground, as the suppression of gravity-driven liquid flow required for solidification feeding.
(4) According to the microstructure and calculations on nucleation rate and growth velocity, the eutectic alloy solidified into Fe_3Si and Fe_2Si as a divorced growth manner.
(5) Apart from divorced growth, the coupled growth appeared under the space condition due to the suppression of long-range solute transport. Meanwhile, the crystal grain size of Fe_3Si phase also increased.

CRediT authorship contribution statement

L. Hu: Writing – review & editing, Writing – original draft, Methodology, Investigation. **W.J. Xie:** Methodology, Investigation, Data curation. **Z.X. Wan:** Methodology, Investigation. **Q.C. Zhong:** Methodology, Data curation. **Y.H. Jing:** Investigation, Data curation. **H.P. Wang:** Writing – review & editing, Validation, Supervision, Conceptualization.

Declaration of competing interest

The authors declare the following financial interests/personal relationships which may be considered as potential competing interests: Wenjun Xie reports financial support was provided by National Natural Science Foundation of China. Liang Hu reports financial support was provided by Shaanxi Natural Science Fund for Distinguished Young Scholar. Haipeng Wang reports financial support was provided by Space Utilization Program of China Manned Space Project. Haipeng Wang reports financial support was provided by National Natural Science Foundation of China. Liang Hu reports financial support was provided by Space Utilization Program of China Manned Space Project. If there are other authors, they declare that they have no known competing financial interests or personal relationships that could have appeared to influence the work reported in this paper.

Acknowledgments

This work was financially supported by the National Natural Science Foundation of China (Grant Nos. 52088101 and 52471048), the Space Utilization Program of China Manned Space Project (Grant No. KJZ-YY-NCL-1-03), and the Shaanxi Natural Science Fund for Distinguished Young Scholar (Grant No. 2023JCJQ30). The authors are very grateful to Professor Y. D. Gu and Professor D. S. Jin for their long-standing advice and supervision. We also appreciate the Chinese astronauts for performing all the space experiments.

References

[1] W. Kurz, M. Rappaz, R. Trivedi, Progress in modelling solidification microstructures in metals and alloys. Part II: dendrites from 2001 to 2018, Int. Mater. Rev. 66 (2020) 30–76.
[2] G. Reinhart, C.A. Gandin, N. Mangelinck-Noël, H. Nguyen-Thi, J.E. Spinelli, J. Baruchel, B. Billia, Influence of natural convection during upward directional solidification: a comparison between in situ X-ray radiography and direct simulation of the grain structure, Acta Mater. 61 (2013) 4765–4777.
[3] H.P. Wang, D.N. Liu, C.H. Zheng, J.F. Zhao, J. Chang, L. Hu, H. Liao, D.L. Geng, W.J. Xie, B. Wei, Spiral eutectic growth dynamics facilitated by space Marangoni convection and liquid surface wave, Phys. Fluids 36 (2024) 047137.
[4] S. Suzuki, K.H. Kraatz, G. Frohberg, Diffusion experiments in liquid Sn-Bi and Al-Ni systems with a stable density layering using the foton shear cell under 1g conditions, Microgravity Sci. Technol. 16 (2005) 120–126.
[5] S. Akamatsu, H. Nguyen-Thi, In situ observation of solidification patterns in diffusive conditions, Acta Mater. 108 (2016) 325–346.
[6] A. Zhang, J.L. Du, Z.P. Guo, S.M. Xiong, Lamellar eutectic growth under forced convection: a phase-field lattice-Boltzmann study based on a modified Jackson-Hunt theory, Phys. Rev. E 98 (2018) 043301.
[7] S. Bottin-Rousseau, V.T. Witusiewicz, U. Hecht, J. Fernandez, A. Laveron-Simavilla, S. Akamatsu, Coexistence of rod-like and lamellar eutectic growth patterns, Scripta Mater. 207 (2022) 114314.
[8] H.P. Wang, H. Liao, J. Chang, D.N. Liu, Q. Wang, M.X. Li, C.H. Zheng, L. Hu, B. Wei, Decoupling effect stimulated independent dendrite growth of eutectic phases under microgravity and containerless states, Mater. Today 75 (2024) 386–392.
[9] G. Ouyang, X. Chen, Y. Liang, C. Macziewski, J. Cui, Review of Fe-6.5 wt%Si high silicon steel—a promising soft magnetic material for sub-kHz application, J. Magn. Magn Mater. 481 (2019) 234–250.
[10] J.S. Shin, J.S. Bae, H.J. Kim, H.M. Lee, T.D. Lee, E.J. Lavernia, Z.H. Lee, Ordering–disordering phenomena and micro-hardness characteristics of B2 phase in Fe–(5–6.5 %)Si alloys, Mater. Sci. Eng. 407 (2005) 282–290.
[11] K. Han, M. Saito, J. Xia, I. Ohnuma, R. Kainuma, Experimental determination of phase diagram involving silicides in the Fe-Si binary system, J. Alloys Compd. 919 (2022) 165810.
[12] S. Cui, I.H. Jung, Critical reassessment of the Fe-Si system, Calphad 56 (2017) 108–125.
[13] L. Hu, W.L. Wang, S.J. Yang, L.H. Li, D.L. Geng, L. Wang, B. Wei, Dendrite growth within supercooled liquid tungsten and tungsten-tantalum isomorphous alloys, J. Appl. Phys. 121 (2017) 085901.
[14] D.C. Van Hoesen, A.K. Gangopadhyay, G. Lohöfer, M.E. Sellers, C.E. Pueblo, S. Koch, P.K. Galenko, K.F. Kelton, Resistivity saturation in metallic liquids above a

dynamical crossover temperature observed in measurements aboard the international space station, Phys. Rev. Lett. 123 (2019) 226601.
[15] R. Novakovic, M. Mohr, D. Giuranno, E. Ricci, J. Brillo, R. Wunderlich, I. Egry, Y. Plevachuk, H.J. Fecht, Surface properties of liquid Al-Ni alloys: experiments vs theory, Microgravity Sci. Technol. 32 (2020) 1049–1064.
[16] C. Koyama, T. Ishikawa, H. Oda, H. Saruwatari, S. Ueno, M. Oshio, Y. Watanabe, Y. Nakata, Densities of liquid lanthanoid sesquioxides measured with the electrostatic levitation furnace in the ISS, J. Am. Ceram. Soc. 104 (2021) 2913–2918.
[17] H.P. Wang, H. Liao, L. Hu, C.H. Zheng, J. Chang, D.N. Liu, M.X. Li, J.F. Zhao, W.J. Xie, B. Wei, Freezing shrinkage dynamics and surface dendritic growth of floating refractory alloy droplets in outer space, Adv. Mater. 36 (2024) e2313162.
[18] N.A. Mauro, A.J. Vogt, K.S. Derendorf, M.L. Johnson, G.E. Rustan, D.G. Quirinale, A. Kreyssig, K.A. Lokshin, J.C. Neuefeind, K. An, X.L. Wang, A.I. Goldman, T. Egami, K.F. Kelton, Electrostatic levitation facility optimized for neutron diffraction studies of high temperature liquids at a spallation neutron source, Rev. Sci. Instrum. 87 (2016) 013904.
[19] L. Hu, L. Wang, M.J. Lin, B. Wei, Single crystal growth and chemical disorder trapping of refractory MoNbReTaW high-entropy alloy solidified under electrostatic levitation state, Metall. Mater. Trans. A 52A (2021) 167–180.
[20] J. Chang, H.P. Wang, H. Liao, D.N. Liu, C.H. Zheng, Q. Wang, M.X. Li, D.D. Zuo, B. Wei, Remarkable undercooling capability and metastable thermophysical properties of liquid Nb84.1Si15.9 alloy revealed by electrostatic levitation in outer space, Rev. Sci. Instrum. 95 (2024) 034501.
[21] M. Felberbaum, M. Rappaz, Curvature of micropores in Al–Cu alloys: an X-ray tomography study, Acta Mater. 59 (2011) 6849–6860.
[22] S. Mukherjee, J. Schroers, Z. Zhou, W.L. Johnson, W.K. Rhim, Viscosity and specific volume of bulk metallic glass-forming alloys and their correlation with glass forming ability, Acta Mater. 52 (2004) 3689–3695.
[23] P. Heintzmann, F. Yang, S. Schneider, G. Lohöfer, A. Meyer, Viscosity measurements of metallic melts using the oscillating drop technique, Appl. Phys. Lett. 108 (2016) 241908.
[24] M.L.N.M. Melo, E.M.S. Rizzo, R.G. Santos, Numerical model to predict the position, amount and size of microporosity formation in Al–Cu alloys by dissolved gas and solidification shrinkage, Mater. Sci. Eng. 374 (2004) 351–361.
[25] J. Lipton, W. Kurz, R. Trivedi, Rapid dridrite growth in undercooled alloys, Acta Metall. 35 (1987) 957–964.
[26] R. Trivedi, P. Magnin, W. Kurz, Theory of eutectic growth under rapid solidification conditions, Acta Metall. 35 (1987) 971–980.
[27] R.W. Hyers, Fluid flow effects in levitated droplets, Meas. Sci. Technol. 16 (2005) 394–401.